Nanoscale Advances

ROYAL SOCIETY OF CHEMISTRY

PAPER

View Article Online
View Journal | View Issue

Cite this: *Nanoscale Adv.*, 2022, **4**, 2189

A freestanding nitrogen-doped MXene/graphene cathode for high-performance Li–S batteries†

Luo Yuanzheng, [a] Ye Zhicheng, [a] Mo Lianghao, [a] Li Buyin [*b] and Li Shufa [*a]

Lithium–sulfur batteries (LSBs) take a leading stand in developing next-generation secondary batteries with an exceptionally high theoretical energy density. However, the insulating nature and undesirable shuttle effect still need to be solved to improve the electrochemical performance. Herein, a freestanding graphene supported N-doped $Ti_3C_2T_x$ MXene@S cathode is successfully synthesized *via* a straightforward no-slurry method. Due to its unique hierarchical microstructure, the MXene-C/S ternary hybrids with high capacity can effectively adsorb polysulfides and accelerate their conversion. Cooperatively, conductive rGO can ameliorate N-MXene nanosheet' restacking, making the lamellar N-Mxene coated sulfur particles disperse uniformly. The assembled Li–S battery with a freestanding $Ti_3C_2T_x$@S/graphene electrode provides an initial capacity of 1342.6 mA h g^{-1} at 0.1C and only experiences a low capacity decay rate of 0.067% per cycle after. Even at a relatively high loading amount of 5 mg cm^{-2}, the battery can still yield a high specific capacity of 684.9 mA h g^{-1} at 0.2C, and a capacity retention of 89.3% after 200 cycles.

Received 28th January 2022
Accepted 25th March 2022

DOI: 10.1039/d2na00072e

rsc.li/nanoscale-advances

1 Introduction

Developing efficient secondary energy batteries is an inevitable requirement of a low-carbon society, most urgently, to help the world move away from fossil fuels. Since high energy density is one of the chief advantages of lithium battery technology, it is expected to meet the ever-increasing requirement for electric vehicles and portable electronics. Commercial Li-ion batteries contain lithium-salt electrolyte, a carbon anode, and lithium-ion embedded compounds such as $LiCoO_2$, $LiMn_2O_4$, and $LiFePO_4$ as the cathode, which are already facing their energy density limit that hinders their further development.[1] As promising next-generation batteries, lithium–sulfur batteries (LiSBs) have raised high hopes to enhance specific capability compared to the state-of-the-art lithium-ion batteries.[2,3] As by-products in the petroleum industry, elemental sulfur has attracted wide attention because of its low cost, non-toxicity and high theoretical capacity.[4] However, there are still several challenges for Li–S batteries, combined with issues originating from the lithium anode, and the as-caused polysulfide shuttling, low sulfur utilization, and short circle life lead to difficulties in commercializing Li–S batteries.[5]

To address these cathodic problems, an effective free-standing strategy that can directly immobilize sulfur in carbon hosts without using the polymer additives and metallic collector has been proposed recently.[6] These novel carbon/sulfur cathodes are promising sulfur hosts to construct cathodes for lithium–sulfur batteries with high utilization and cycling stability of active materials. Pei developed a two-dimensional (2D) graphene self-supporting hollow nanostructure, which was synthesized by reacting sodium thiosulfate with hydrochloric acid.[7] This prefabricated free-standing carbon film based on a facile chemical deposition method (*i.e.*, $Na_2S_2O_3 + 2HCl \rightarrow 2NaCl + SO_2 + H_2O + S$) has been explored to achieve uniform sulfur loading. However, due to the weak interaction between low polar carbon and high polar LiPS, the physical isolation and adsorption provided by carbon-based materials have limited effect on inhibiting battery capacity decay, especially for high sulfur loaded electrodes.[8,9]

Quite similar to graphene, 2D transition metal carbides (MXenes) with rich surface functionality and high conductivity, are one of the promising candidates of high-performance electrode materials for Li–S batteries.[10–13] As opposed to graphene, the delaminated MXenes with a low specific surface area but having a unique hydrophilic surface and active polar sites could effectively entrap and transform LiPS species.[14,15] Bao *et al.* prepared a crumpled nitrogen-doped $Ti_3C_2T_x$ MXene nanosheet/sulfur composite *via* a sulfur melting diffusion method.[16] Melamine as a nitrogen source and spacer endows the electrodes with a high specific surface area and effectively promotes polar surface properties. These N-$Ti_3C_2T_x$ MXene/

[a]School of Electronic Information Engineering, Guangdong Ocean University, China. E-mail: lishufa@gdou.edu.cn

[b]School of Optical and Electronic Information, Huazhong University of Science and Technology, China

† Electronic supplementary information (ESI) available. See DOI: 10.1039/d2na00072e

sulfur composite electrodes also presented a high reversible capacity of 1144 mA h g^{-1} at a 0.2C rate, a high level of capacity retention of 950 mA h g^{-1} after 200 cycles and extended cycling stability.

On the other hand, various hybridizations of metallic compounds with graphene materials have been designed.[17] Many of these metal/carbon composite substrates exist as an agglomeration of sulfur particles. Xiao *et al.*[18] developed a nanodot $Ti_3C_2T_x$ MXene-based electrode with rich surface polar nanodot sites, which exhibits an almost theoretical discharge capacity at a medium sulfur loading of 1.8 mg cm^{-2}. Hybridizing 2D MXenes and graphene is also one of the promising strategies to inhibit the restacking of MXene nanosheets. Li *et al.*[19] developed curved and reduced graphene oxide (rGO)/MXene hybrid fibres that showed a practical chemical anchoring effect on LiPSs through interfacial Ti–S interactions. Meanwhile, 3D porous graphene could exert its large pore volume and high surface area to accommodate solid charge/discharge products of S/Li_2S. Song *et al.*[20] constructed a free-standing porous $Ti_3C_2T_x$ MXene-C/S ternary hybrid aerogel through a straightforward hydrothermal method followed by lyophilization. The $Ti_3C_2T_x$ MXene used as additives significantly suppresses LiPS shuttling and expedites sulfur utilization, thus leading to a high capacity of 1270 mA h g^{-1} at 0.1C and a stable cycling performance at 1C up to 500 cycles. Therefore, developing novel MXene nanostructures with a porous framework and heteroatom doping would be desirable to boost the Li–S battery performances but remains a significant challenge thus far. Inspired by those previous studies, we report a nitrogen-doping strategy for functionalizing MXene nanosheets by introducing heteroatomic nitrogen into a 3D porous MXene-C/S ternary composite as a free-standing sulfur cathode.

Herein, we utilized melamine nanospheres as a nitrogen source to achieve the N-doping on the $Ti_3C_2T_x$ surface and added the N-MXene nanosheets into the colloidal sulfur solution as a polar precursor; thereafter combining this unique precursor with 3D interconnected rGO to assemble the N-$Ti_3C_2T_x$ MXene@S/rGO (NMSG) composite as a free-standing electrode *via* a straightforward hydrothermal method. Unlike non-polar material that contact and load active materials first, the sulfur element formed in colloidal solution was taken forthwith to accommodate a polar N-$Ti_3C_2T_x$@S surface, which can efficiently anchor sulfur species to restrict shuttle effects *via* Ti–S interaction. The optimum N-$Ti_3C_2T_x$@S/G cathode exhibited superior electrochemical performance, including a high capacity of 1320 mA h g^{-1} at 0.1C, a stable cycling performance at 0.2C up to 300 cycles (ultraslow capacity decay of 0.12% per cycle), and a high sulfur loading of 3.8 mg cm^{-2}.

2 Experimental section

2.1 Preparation of GO and $Ti_3C_2T_x$ MXene

The graphene oxide (GO) was synthesized by the method reported before.[21] The $Ti_3C_2T_x$ nanosheets were prepared through HF etching and exfoliation of the MAX phase precursor. Typically, lithium fluoride (1.6 g) was dissolved in 20 mL concentrated 9 M HCL solution with magnetic stirring to dissolve the lithium fluoride. In order to avoid a severe exothermic reaction, add 500 mL ice water to the water bath kettle to cool the etchant. After the reaction had proceeded for 1 h, 1 g of Ti_3AlC_2 was slowly introduced into the above solution under continuous stirring at room temperature for 24 h. Dilute hydrochloric acid of 1 M concentration was repeatedly added to wash the excess lithium fluoride impurities 3 times. The obtained solid precipitate was centrifuged to separate the precipitate and washed several times until the pH value of the supernatant was equal to 7. The $Ti_3C_2T_x$ nanosheets were finally attained by vacuum drying at 60 °C overnight.

2.2 Synthesis of melamine–formaldehyde (MF) resin spheres

MF spheres were synthesized *via* a precipitation polymerization method.[22] Typically, 25 mL deionizing water and 3 mL methanol were added to a 50 mL three-mouth flask, and 1 g melamine was weighed and homogeneously dispersed under stirring. After 10 min, 3 mL formaldehyde was added, and the pre-polymerization reaction was 0.5 h. Subsequently, 0.25 mL formic acid diluent was added as a catalyst. After 20 min, the solution becomes turbid, and the reaction continues for 2 h to obtain a milky turbid solution. Then the product was washed and cleansed with anhydrous ethyl alcohol and deionizing water 4 times, placed in a baking oven, dried at 60 °C, and white powder monodisperse MF microspheres were obtained.

2.3 Synthesis of N-$Ti_3C_2T_x$ nanosheets

The N-$Ti_3C_2T_x$ nanosheets were prepared through a sacrificial template method. The as-obtained $Ti_3C_2T_x$ suspension (5 mg mL^{-1}, 20 mL) and MF dispersion (10 mg mL^{-1}) were mixed together and sonicated for 30 min. Next, the mixture was centrifuged at 5000 rpm for 5 min to collect the solid intermediate product. Additionally, the ratios of MF : $Ti_3C_2T_x$ (4 : 1) were prepared by adjusting the weight of MF. The precipitates were collected by centrifugation, and washed with ethanol to remove impurities. After freeze-drying, uniform nitrogen doped samples can be obtained by removing the MF spheres *via* annealing at 600 °C for 1.5 h at a heating rate of 5 °C min^{-1} in atmosphere.

2.4 Preparation of the sulfur cathodes

A one-step lyophilization and reduction was used to obtained the cathodes. Typically, 16 mg of N-Ti_3C_2 powder and 158 mg of $Na_2S_2O_3$ were mixed with 18 mL deionized water and sonicated for 10 min. Notably, the N-MXene and reaction-generated colloidal sulfur need a mass ratio of 1 : 2 for the best dispersion effect. Then, 2 mL dilute hydrochloric acid (1 mol mL^{-1}) was added drop-wise to the above solution with magnetic stirring. The generated sulfur particles are loaded and coated with lamellar N-MXene, and the solution is gradually transformed into blue-purple floccules (Fig. S1†), which indicates the continuous formation of colloidal sulfur through the Dundar phenomenon. The colour of colloidal sulfur is no longer visible, implying that the sulfur particles are homogeneously coated by N-Ti_3C_2. The total time of dropping and the reaction was controlled at about 2 h. After the solution was quiescent for 12 h

at room temperature, the supernatant was removed, and the precipitate was lyophilized and mixed with 5 mg mL^{-1} GO by ultrasonic dispersion. The N-MX@S/GO suspension was further reduced *via* a hydrothermal process at 120 °C for 12 h. After freeze-drying, the N-MX@S/G monolith was obtained. The bulk electrode composite was compressed into a 10 mm diameter round sheet by using a hydraulic tablet press at 1 MPa. Since the areal sulfur loading of $Ti_3C_2T_x$ foam/S cathodes could be easily controlled by adjusting the mass of $Na_2S_2O_3$, three typical N-Ti_3C_2@S/graphene cathodes with areal sulfur loadings of 1.5, 5.1, and 6.0 mg cm^2 (denoted as NMSG-1.5, -5.1, and -6.0, respectively) were prepared. For comparison, the other electrodes were prepared using the same method as above, replacing the N-$Ti_3C_2T_x$ MXene with pure $Ti_3C_2T_x$ in the first step, denoted as the MSG electrode.

2.5 Materials characterization

The morphologies and microstructures of the NMSG and MSG samples were observed using a Hitachi (SU8010) scanning electron microscope. TEM observations were performed with a JEOL JEM-2100F TEM equipped with an energy dispersive spectrometer (EDS) device at 200 kV. The NMSG and MF samples were characterized using an Escalab 250Xi X-ray photoelectron spectroscope (XPS). X-ray powder diffraction (XRD) patterns were collected on a Rigaku SmartLab with CuKa radiation at a generator voltage of 40 kV.

2.6 Coin cell assembly and electrochemical tests

All the symmetric cells were assembled in an Ar-filled glove box, with the as-prepared electrodes as the cathodes, polypropylene (PP) films as the separators, and lithium foil as the anodes. The specific capacity of the cathode sheets was determined in half cells by the elemental sulfur. The electrolyte was 1 M lithium bis(trifluoromethane sulfonyl) imide (LiTFSI) in 1,3-dioxolane (DOL) and 1,2-dimethoxyethane binary solvents (1 : 1 by volume) containing 1 wt% $LiNO_3$ as an additive. 60 L electrolyte was added to each cell. Cyclic voltammetry (CV) was carried out at scan rates of 0.1 and 1 mV s^{-1}. The galvanostatic charge–discharge test was carried out on battery test systems (CT3002A, LAND) with a voltage range of 1.7–2.8 V. Cyclic voltammetry (CV) measurements and electrochemical impedance spectroscopy (EIS) were conducted using an electrochemical work station (Chenhua CHI 660). All the electrochemical tests were performed at room temperature.

3 Results and discussion

Fig. 1 shows the synthetic procedure of the N-MXene@S/G (NMSG) aerogel electrodes based on a sacrificial templating method followed by a reduction process with co-assembly of rGO flakes onto the sulfur particles. The schematic diagram of the N-doped Mxene preparation process is shown in Fig. 1a. First, the few-layered and organ-like $Ti_3C_2T_x$ flakes (Fig. 1b) were obtained *via* treating a commercial MAX-phase Ti_3AlC_2 precursor using a LiF/HCl etchant. The dispersed $Ti_3C_2T_x$ nanosheets spontaneously wrapped on the melamine–

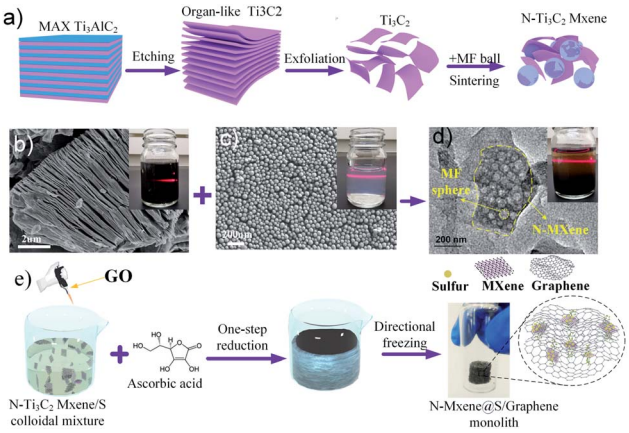

Fig. 1 (a) Schematic illustration for the synthesis of N-$Ti_3C_2T_x$ MXene nanosheets; (b–d) corresponding SEM and TEM images of $Ti_3C_2T_x$ flakes, the MF nanosphere and the $Ti_3C_2T_x$ wrapped MF nanosphere; (e) schematic of the one-step synthesis process of the freestanding N-MXene@S/G composite.

formaldehyde (MF) nanospheres, as shown in Fig. 1c and d. Then, the intermediate precipitate was further annealed at 500 °C in Ar for 2.5 h, leading to the removal of the nanosphere template. Although the MXene has hydroxyl or terminal oxygen on its surface, making part of the preparation method of graphene-derived porous materials suitable for MXenes. However, the pure $Ti_3C_2T_x$ is readily precipitated, making it difficult to anchor sulfur nanoparticles between the layers compared to graphene nanosheets. The N-$Ti_3C_2T_x$ nanosheets could easily disperse in a GO suspension, and loading sulfur *in situ* during the formation of colloid sulfur enables fast electrochemical reaction kinetics. Combined with digital photographs of the Dundar phenomenon in solution, the results of HR-TEM and SEM suggest that the obtained $Ti_3C_2T_x$-modified layer has dispersibility and can further form a sandwich-like N-MXene hybrid structure in a straightforward manner. A one-step hydrothermal reduction and freeze casting method was applied to prepare the freestanding sulfur electrode. The N-doped MXene coated sulfur nanoparticles (N-MXene@S) were dispersed and anchored in the graphene aerogel matrix during this simple precipitation and hydrothermal reduction process, and the N-MXene@S nanoparticles are decorated on the rGO sheets. After freeze-drying, the micron-sized conductive network of rGO facilitates fast lithium-ion diffusion and electron transfer, and the highly active polar surface of N-$Ti_3C_2T_x$ MXene can efficiently anchor nanoscale sulfur species to restrict shuttle effects *via* Ti–S interaction and enhance the cycling stability of Li–S batteries. Meanwhile, this ternary N-MXene@S/G (NMSG) composite structure was able to adsorb polysulfides and effectively inhibit the "shuttle effect" through the dual effects of functional groups and metal–sulfur bonding.

The morphologies of the N-MXene@S/G sample were observed by scanning electron microscopy (SEM). As shown in Fig. 2a, the dimension of graphene nanosheets was about 200–500 μm, while N-MXene@S nanoparticles had a diameter of 100–250 nm. It is noteworthy that these sulfur-loaded heterostructures

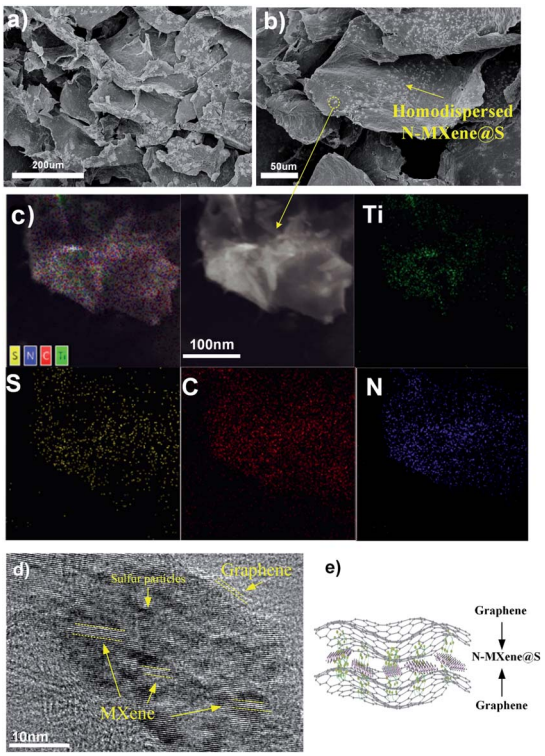

Fig. 2 (a, b) FESEM image of the N-MXene@S/G composite. (c) HRTEM image and EDS spectrum mapping: Ti, S, C, and N elemental distribution of the N-MXene@S/G composite; (d) HRTEM image of the N-MXene@S/G composite; (e) schematic diagram of the sandwich structure in the N-MXene@S/G composite.

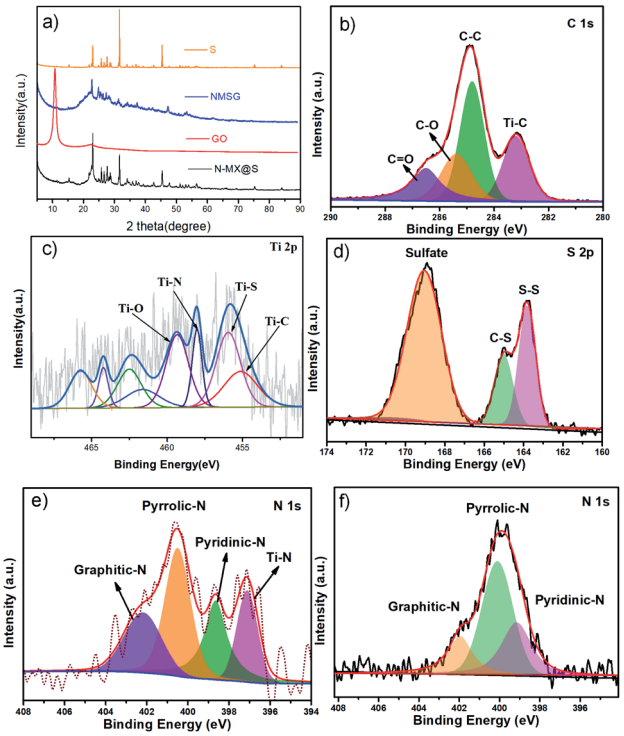

Fig. 3 (a) XRD of pure sulfur, GO, N-MXene@S/G and N-MXene@S; high-resolution XPS survey of NMSG: C 1s (b) spectrum, Ti 2p (c) spectrum, S 2p (d) spectrum and N 1s (e) spectrum. (f) N 1s (e) spectrum of a MF nanosphere.

are decorated uniformly on the surface of the graphene sheets (Fig. 2b). Meanwhile, the hierarchical porous structure of graphene facilitates rapid diffusion to take place and provides adequate space to accommodate the volumetric change of the MXene encapsulated sulfur. To understand the potential benefits of sulfur dispersion with high concentration N-MXene, we found that the N-MXene@S cathodes with a sulfur loading mass of 1.5 mg cm^{-2} could produce the most homogeneous structure. The N-$Ti_3C_2T_x$ nanosheet encapsulated sulfur particles were also investigated by element mapping (EDX), as shown in Fig. 2c. For their application in Li–S batteries, sulfur being distributed homogeneously is critical to the high sulfur utilisation. The HR-TEM image (Fig. 2d) reveals parallel and ordered lattice fringes with sulfur particles, which demonstrates the coexistence of $Ti_3C_2T_x$ MXene and rGO. Fig. S3 in the ESI† shows the TEM image of the uniformly dispersed sulfur nanoparticles encapsulated by Mxene. A schematic drawing of the sandwich-like N-MXene@S/G hybrid structure for the free-standing sulfur electrode is shown in Fig. 2f. This sandwich framework serves as a conductive matrix and effectively restrains volume expansion and blocks the diffusion of polysulfides, leading to the high utilisation of sulfur.

Fig. 3a shows the XRD spectra of colloidal sulfur, GO, N-MX@S and NMSG. Both NMSG and MSG exhibited three dominant peaks at 23.4°, 26.0°, and 27.7°, suggesting that sulfur was anchored on the surface of graphene and MXene nanosheets. Moreover, a broad peak (24°) was found in NMSG, indicating that

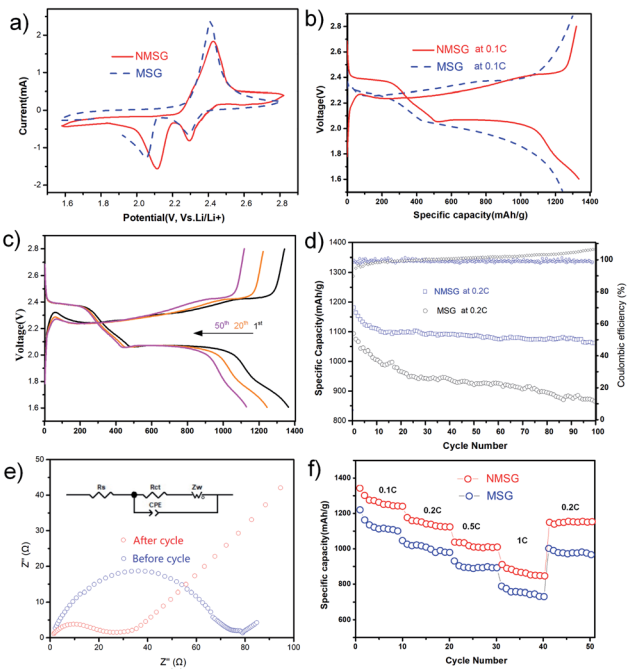

Fig. 4 Electrochemical performance of Li–S cells. (a) CV curves of NMSG and MSG and (b) the charge–discharge curves of NMSG and MSG at 0.1C; (c) the charge–discharge curves of NMSG at 0.1C with the 50th cycle (d) cycling performance at 0.2C (e) Nyquist plots, and (f) rate performance of NMSG and MSG.

GO was reduced to rGO. The titanium, carbon, nitrogen, and sulfur elements were further characterized, and their corresponding XPS spectra are displayed in Fig. 3b–f. In Ti2p spectra (Fig. 4c), two obvious peaks at 461.44 and 455.29 eV were assigned to the 2p1/2 and 2p3/2 signals of the $Ti_3C_2T_x$ MXene.[23] Notably, the Ti–C bond was found for MXene in high-resolution C 1s (281.9 eV) and Ti 2p (459.2 eV and 455.4 eV) spectra (Fig. 2c and d). Moreover, the N 1s spectra of NMSG and MF are shown in Fig. 3f. The N 1s spectrum of the MF sample shows three peaks at 402.2, 398.3, and 399.8 eV, which correspond to graphitic-N, pyridinic N, and pyrrolic N. Moreover, Ti–N bonds (397.0 eV) were observed in the N 1s spectra of NMSG. These results further verified successful nitrogen doping into the $Ti_3C_2T_x$ nanosheets. As far as is known, N dopants can efficiently enhance the interaction with sulfur/polysulfides and electrochemical reactivity.[14]

To investigate the electrochemistry of the as-prepared freestanding electrode, N-MXene@S/G composites with a sulfur loading mass of 1.5 mg cm^{-2} were pressed into sheets at 5 MPa and directly used as a cathode without an extra slurry coating or polymer additives to assemble the Li–S half cell (Fig. S1†). The cyclic voltammetry (CV) measurements of N-MX@S/G and MX@S/G were performed from 1.5 to 2.8 V with a scan rate of 0.1 mV s^{-1}. Two distinct reduction peaks at 2.33 and 2.02 V correspond to the conversion of sulfur to soluble LPSs and insoluble Li_2S, respectively. The oxidation peak at 2.4 V is attributed to the multistep conversion of Li_2S/Li_2S_2 to LPSs and sulfur. Obviously, the reduction peaks of Li–S cells with NMSG-1.5 electrodes exhibited higher potentials than those of Li–S cells with MSG electrodes, indicating the better redox reaction kinetics of LPS owing to heteroatomic doping.

The promoted sulfur electrochemistry is further proved by the charge/discharge profiles of NMSG-1.5 electrodes (Fig. 4b). High initial discharge capacities of 1342.6 mA h g^{-1} were achieved in the potential range from 1.6 to 2.8 V at a 0.1C rate (1C = 1673 mA h g^{-1}). The advantages of NMSG also deliver two stable discharge potential plateaus, corresponding to the smooth transformation of the liquid-to-solid reduction reaction of sulfur. This strong LiPS-trapping ability not only contributes to an acceleration of LiPS redox reactions from short-chain LiPS to Li_2S_2 and Li_2S but also endows a higher potential plateau in discharge curves, which agrees well with the above CV analysis. Moreover, this property was observed even after 50 cycles, indicating high reversibility of the NMSG-1.5 electrode as shown in Fig. 4c. Moreover, the sulfur content in the composite was calculated to be 52.9 wt% by thermogravimetric analysis (TGA), as shown in Fig. S2.†

Fig. 4d shows the cycling performance of NMSG-1.5 and MSG composite electrodes at 0.2C. The two cathodes both showed a high initial discharge capacity of 1092.5 mA h g^{-1} and 1180.7 mA h g^{-1}, respectively. The discharge capacity of the bare Ti_3C_2@S/G electrodes decreased to 955.1 mA h g^{-1} within just 30 cycles. The fast capacity decay could be due to the lack of effective polar chemical adsorption. In contrast, the N-Ti_3C_2@S composite electrode achieved a high reversible capacity of 1068.9 mA h g^{-1} which was retained after 100 cycles, corresponding to a low fading rate of 0.094% per cycle with an average coulombic efficiency over 99%.

Electrochemical impedance spectra (EIS) of the NMSG cathode before and after cycling were obtained to investigate its performances further, as shown in Fig. 4e. Before cycling, the Nyquist plot (Fig. 4b) showed a high-frequency intersection, which corresponded to a charge-transfer resistance close to 50. This could be attributed to the resistance from the electrolyte that has not fully penetrated the nanostructure as well as the lack of a highly conductive (metallic) current collector (*i.e.*, aluminium foil). After 5 cycles, the value of the charge transfer resistance further decreases to 50, attributed to the fast charge transport in NMSG-1.5. The charge transfer resistance is significantly lower than that of conventional slurry-based cathodes (120 *vs.* 580), which indicates good electrochemical reversibility between electron-transporting pathways generated after the electrolyte penetrated the macroporous 3D N-MXene/graphene network.

The rate performance of NMSG-1.5 and MSG cathodes at various currents from 0.1C to 1C were also investigated, as shown in Fig. 4f. The NMSG monolith cathode with uniformly dispersed N-MX@S particles delivers a higher reversible capacities of 1342.6, 1180.7, 1035.1, 973.1, and 733.3 mA h g^{-1} at 0.1, 0.2, 0.5, 1, respectively. When the current density shifted back to 0.2C, it still remained at a high discharge capacity of 1146.2 mA h g^{-1}. However, MSG electrodes presented lower rate capacities, indicating enhanced charge transfer with doped nitrogen.

In addition, the CV peaks converge and nearly overlap within 3 cycles, as shown in Fig. 5a, suggesting good electrochemical reversibility after the cell equilibrated and the electrolyte penetrated the macroporous graphene structure. The CV curves at different scanning rates from 0.2 mV s^{-1} to 1 mV s^{-1} were obtained (Fig. 5b). Long-term cycling at 1C-rates demonstrated the cyclability of NMSG-1.5 cathodes, as shown in Fig. 5c. The as-designed N-MXene@S/G and MXene@S/G cells exhibit a high initial capacity of 905.8 mA h g^{-1} and 852.1 mA h g^{-1} at 1C, respectively. However, the cell with MSG undergoes a fast capacity decay in the first 25 cycles, ending with 263 cycles with a low capacity of 523.6 mA h g^{-1}. Impressively, the cell with NMSG-1.5 delivers a discharge capacity of 721.7 mA h g^{-1} after 300 cycles (96% average coulombic efficiency), corresponding to a much lower fading rate of 0.067% every cycle. To further understand the improved electrochemical performance of the N-MXene@S/G composite, Fig. 5d shows the cycling performance of the NMSG electrode with high sulfur loadings of 5.1 mg cm^{-2} and 6.0 mg cm^{-2}. Fig. S4† shows the SEM images of the composites with different areal sulfur loadings. In contrast, a lower capacity of loading greater than 6.0 mg cm^{-2} was obtained, which is responsible for the inadequate surface contact between the active materials and the liquid electrolyte.[24] Upon cycling at 0.2C, the NMSG-5.1 electrode can exhibit a discharge capacity of 611.6 mA h g^{-1} after 200 cycles. The initial capacity decreases with increasing sulfur loading, with the 1.5 mg cm^{-2} electrodes achieving 1342.6 mA h g^{-1} (2.1 mA h cm^{-2}) *versus* 684.9 mA h g^{-1} (4.2 mA h cm^{-2}) for the 5.1 mg cm^{-2} electrodes. Such a high areal capacity is superior to that reported recently for lithium-ion batteries (4 mA h cm^2),[25] demonstrating the practical potential of the freestanding NMSG electrode.

These results show that polarization does not increase significantly at a high sulfur load. Density functional theory

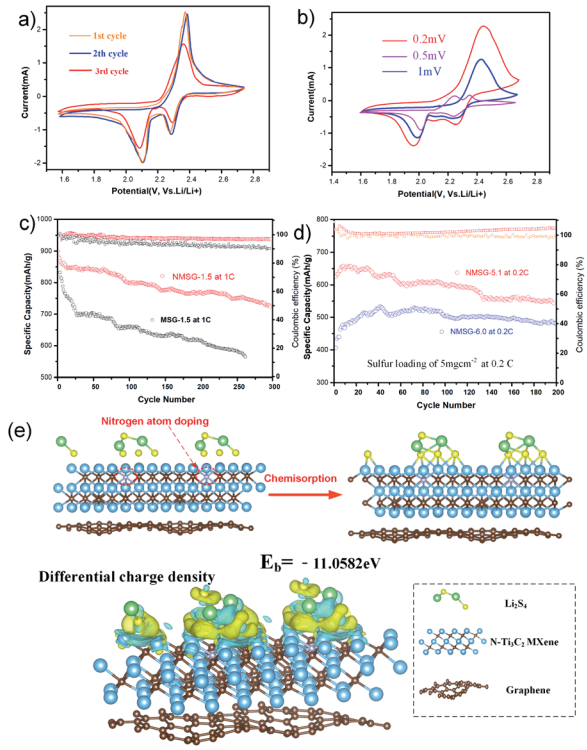

Fig. 5 (a) The first-third CV curves of NMSG cathodes at 0.1 mV s; (b) CV curves of NMSG at various scan rates; (c) long term cycling performances of the Li–S cell with NMSG at 1C for 300 cycles; (d) cycling performances of the NMSG electrode and MSG electrode with a 5.1 mg cm^{-2} sulfur loading at 0.1C for 100 cycles; (e) the optimized structures and adsorption energies of Li_2S_4 on the N-Ti_3C_2 surfaces.

(DFT) results could further explain the excellent long-term stability performance. Fig. 4e shows that the chemical interaction between Li_2S_4 and N-Ti_3C_2 (11.05 eV) is stronger than that of the corresponding Ti_3C_2 (10.59 eV). The high binding energy represents the energetically favourable formation of chemical bonds and enhanced chemisorption of polysulfide by N-Ti_3C_2 MXene. The capacity decay rate is also compared with other MXene-C/S ternary hybrid cathodes, and the details are shown in Table S1,† the N-doped MXene@S/G ternary hybrid shows the advantage of cycle stability. Especially, the performance of the NMSG cathode is superior to most of the previously reported MXene/G composite cathodes. Overall, the unique electrochemical properties of NMSG are attributed to the three following reasons: (1) the hybrid conductive network structure of graphene/MXene nanosheets ensures fast electron transport; (2) sulfur was homogeneously encapsulated and dispersed between graphene and MXene nanosheets; (3) the enhanced polarity of the N-MXene host effectively minimizes the "shuttle effect" and allowing high sulfur utilization.

4 Conclusion

In summary, we synthesized novel three-dimensional N-MXene/graphene sulfur hosts through a facile no-slurry method. The as-prepared freestanding ternary N-MXene-@S/G cathodes exhibited stable cycling performances, including a high reversible capacity of 1180.7 mA h g^{-1} at a 0.2C rate and a high level of capacity retention of 1068.9 mA h g^{-1} after 100 cycles. Even under a relatively high loading amount of 5.2 mg cm^{-2}, the battery can still yield a high specific capacity of 721.7 mA h g^{-1} at 0.1C, and a capacity retention of 579.6 mA h g^{-1} after 300 cycles. The improved electrochemical performance is attributed to graphene macropores facilitating electrolyte diffusion to sulfur for redox reactions, and heteroatom doping of the MXene nanosheets effectively minimized the shuttle effect. Overall, the simple fabrication of these binder-free, freestanding MXene-based cathodes presents tremendous potential for application in high-performance Li–S batteries.

Conflicts of interest

There are no conflicts to declare.

Acknowledgements

The authors acknowledge the support from the "Guangdong Basic and Applied Basic Research Foundation" (Grant No. 2020A1515111179), "Research Platform and program of Guangdong Colleges and Universities-Youth Project" (Grant No. 2020KQNCX027) and Zhanjiang Innovation and Entrepreneurship Team introduced the "Pilot Plan" project "Key Technology of Underwater Acoustic Monitoring and Target Detection of Deep Sea Cage" (Grant No. 211207157080994).

Notes and references

1 F. Wu, J. Maier and Y. Yu, *Chem. Soc. Rev.*, 2020, **49**(5), 1569–1614.
2 T. Li, X. Bai, U. Gulzar, *et al.*, *Adv. Funct. Mater.*, 2019, **29**(32), 1901730.
3 L. Yang, Q. Li, Y. Wang, Y. Chen and Y. Zhong, *Ionics*, 2020, **26**, 1–20.
4 J. Chai, J. Du, Q. Li, N. Han, W. Zhang and B. Tang, *Energy Fuels*, 2021, **35**, 15455–15471.
5 K. Rudra, J. Liu, H. Jang-Yeon and Y. K. Sun, *J. Mater. Chem. A*, 2018, **6**(25), 11582–11605.
6 L. Zhou, D. L. Danilov, R. Eichel and P. H. L. Notten, *Adv. Energy Mater.*, 2021, **11**(15), 2001304.
7 F. Pei, L. Lin, D. Ou, Z. Zheng, S. Mo, X. Fang and N. Zheng, *Nat. Commun.*, 2017, **8**, 482.
8 J. Li, Y. Qu, C. Chen, X. Zhang and M. Shao, *Nanoscale*, 2021, **13**, 15–35.
9 L. Lu, F. Pei, T. Abeln and Y. Pei, *Carbon*, 2020, **157**, 437–447.
10 X. Song, H. Wang, S. Jin, M. Lv and J. Xu, *Nano Res.*, 2020, **13**, 9.
11 Y. Aierken, C. Sevik, O. Gulseren, F. M. Peeters and D. Cakir, *J. Mater. Chem. A*, 2018, **6**, 2337–2345.
12 Y. Liu, J. Yu, D. Guo, Z. Li and Y. Su, *J. Alloys Compd.*, 2019, **815**, 152403.
13 R. Meng, Q. Deng, C. Peng, B. Chen and J. Yang, *Nano Today*, 2020, **35**, 100991.

14 Z. Xiao, Z. Li, X. Meng and R. Wang, *J. Mater. Chem. A*, 2019, **7**, 22730–22743.
15 P. Liu, L. Qu, X. Tian, Y. Yi, J. Xia, T. Wang, J. Nan, P. Yang, T. Wang, B. Fang, *et al.*, *ACS Appl. Energy Mater.*, 2020, **3**, 2708–2718.
16 W. Bao, L. Liu, C. Wang, S. Choi, D. Wang and G. Wang, *Adv. Energy Mater.*, 2018, **8**, 1702485.
17 S. Zhou, J. Lan, K. Song, Z. Zhang, J. Shi and W. Chen, *FlatChem*, 2021, **28**, 100259.
18 X. Zhubing, L. Zhonglin, L. Pengyue, X. Meng and R. Wang, *ACS Nano*, 2019, **13**, 3608–3617.
19 H. Li, F. Shao, X. Wen, Y. Ding and N. Hu, *Electrochim. Acta*, 2021, 137838.
20 J. Song, X. Guo, J. Zhang, Y. Chen, C. Zhang, L. Luo, F. Wang and G. Wang, *J. Mater. Chem. A*, 2019, **7**(11), 6507–6513.
21 L. Yz, W. Yq, H. J and L. By, *Mater. Des.*, 2021, **203**, 109612.
22 Z. Fan, C. Wei, L. Yu, Z. Xia, J. Cai, Z. Tian, G. Zou, S. X. Dou and J. Sun, *ACS Nano*, 2020, **14**, 867–876.
23 T. Zhao, P. Zhai, Z. Yang, J. Wang, L. Qu, F. Du and J. Wang, *Nanoscale*, 2018, **10**, 22954–22962.
24 J. H. Yun, J. H. Kim, D. K. Kim and H. W. Lee, *Nano Lett.*, 2018, **18**, 475–481.
25 D. Gastol, M. Capener, C. Reynolds, C. Constable and E. Kendrick, *Mater. Des.*, 2021, **205**, 109720.